Mechanics Research Communications 136 (2024) 104233

Contents lists available at ScienceDirect

Mechanics Research Communications

journal homepage: www.elsevier.com/locate/mechrescom

Nonlinear dynamics and chaos of a waterbomb origami unit-cell considering different symmetry conditions

Guilherme V. Rodrigues, Marcelo A. Savi *

Universidade Federal do Rio de Janeiro, COPPE - Department of Mechanical Engineering, Center for Nonlinear Mechanics, 21.941.972 Rio de Janeiro RJ, Brazil

ARTICLE INFO

Keywords:
Origami
Waterbomb pattern
Unit-cell
Nonlinear dynamics
Chaos
Symmetry

ABSTRACT

Origami has been inspirating the development of novel engineering systems and structures. The traditional waterbomb folding pattern is one of the most widely employed pattern and its description from the unit-cell is related to multiple degrees of freedom (DoF) systems. This work investigates the nonlinear dynamics and chaos of a waterbomb origami through its unit-cell, considering different symmetry hypotheses that simplify its kinematics, resulting in 1-DoF and 2-DoF dynamical systems. The investigation starts with a kinematic analysis of the waterbomb folding pattern and afterward, a reduced-order dynamical model with lumped masses on vertices and torsional springs on creases is built. Symmetry assumptions are discussed, identifying the differences induced by either geometrical nonlinearities or external stimuli. Numerical simulations are carried out showing details of the system nonlinear dynamics, showing intricate situations such as chaos. The comparison among different symmetry conditions provides a qualitative picture of the system dynamics, showing significative differences and highlighting the importance of the origami mechanical behavior comprehension, its modeling and nonlinear dynamics for a proper design of origami-inspired systems.

1. Introduction

Origami is the ancient art of paper folding that consists of folding a sheet of paper to build a shape that can be either abstract or representative of realistic objects. The goal is to build a three-dimensional structure from a two-dimensional sheet source exclusively through folding operations. Although its original purpose conventionally perceived recreational and artistic, over the years origami has intrigued scientists to investigate its underlying principles.

In the last decades, it was discovered that several shapes could be created using traditional origami [21]. The origami mathematics increased the number and sophistication of origami models, which connected the origami knowledge with engineering solutions [17,18]. These discoveries enabled new approaches for manufacturing, assembling, and morphing of devices and structures based on origami principles [10].

Nowadays, origami-inspired systems and structures have been increasingly adopted across a wide range of scales, from nano-scale - as in DNA applications [35], to giga-scale - as in space structures [29]. Distinct fields of knowledge are of concern including areas as biomedical [2], material science [26], architecture and civil engineering [30], mechanical engineering [36], among others. These structures withhold some origami inherent properties as high compactability [7], stretchability without deformation [4] and adaptive mechanical properties [9]. The main idea is the use of reconfigurable properties [12], especially to fit large structures into small spaces. Therefore, potential advantages of origami-inspired structures include deployability, reconfigurability, tunability, scalability and self-actuation [31].

In general, the description of origami systems is a complex task due to the large number of degrees of freedom (DoFs). Such description can be made by considering either kinematic or mechanical approaches. Fonseca *et al.* [15] presented a general overview of origami-inspired systems and structures discussing their fundamentals, applications, and modeling approaches. It was discussed either kinematic- and mechanic-based formulations. Reduced-order models were presented as an interesting strategy to deal with the complex behavior of origami-inspired systems, being essentially related to symmetry conditions. Furthermore, nonlinear dynamics were exploited.

Dynamical analysis of origami systems is a challenging topic that has been treated only recently [34]. Since the origami is a slender structure with a complex geometry, stability analysis is an essential part of the origami design and consequently, dynamical behavior is an important

* Corresponding author.
E-mail address: savi@mecanica.coppe.ufrj.br (M.A. Savi).

https://doi.org/10.1016/j.mechrescom.2023.104233
Received 6 January 2023; Received in revised form 6 July 2023; Accepted 5 December 2023
0093-6413/© 2023 Elsevier Ltd. All rights reserved.

issue to be investigated [1,24,37]. Geometrical and constitutive nonlinearities make origami dynamical behavior a rich and complex research topic.

The waterbomb folding pattern has been widely studied [6,14,27] and employed in several origami-inspired structures [16,34] due to its exceptional characteristics as a tubular origami [11,28]. Since these structures are composed of a tessellation of several unit-cells, the analysis of a single waterbomb origami unit-cell is an essential point of the analysis of these structures [15,33].

Usually, the kinematics of the waterbomb pattern is simplified by assuming a symmetric unit-cell, leading to a 1-DoF system [5,11,28]. Rodrigues *et al.* [34] and Fonseca *et al.* [16] investigated the nonlinear dynamics of a 1-DoF waterbomb-based structure. The kinematic analysis of a waterbomb tessellation with 2-DoF model has been performed by Rodrigues & Savi [33] and Imada & Tachi [19], but the nonlinear dynamics of this structure is not explored [15].

This work deals with the nonlinear dynamics of a waterbomb origami unit-cell by considering different symmetry conditions, defining distinct degrees of freedom dynamical systems: 1-DoF and 2-DoF unit-cell models. Asymmetric conditions are induced by either geometrical nonlinearities or external stimuli, showing the importance of the modeling issues to develop proper designs. A kinematic analysis is developed to build a reduced-order dynamical model based on the unit-cell behavior, considering lumped masses on vertices and torsional springs on creases. Numerical simulations explore details of the origami nonlinear dynamics considering different symmetry conditions, and three cases are of concern: Case 1 - symmetric waterbomb unit-cell subjected to symmetric stimuli (1-DoF system); Case 2 - symmetric unit-cell subjected to asymmetric external stimuli (2-DoF system); and Case 3 - plane-symmetric unit-cell subjected to symmetric external stimuli (2-DoF system). Results show intricate nonlinear dynamics including chaos and significative differences according symmetry conditions.

2. Waterbomb origami

A *folding pattern*, or *crease pattern*, is the arrangement of folding lines within the domain, such as a flat sheet of paper, being defined by *creases, vertices*, and *panels* (or *facets*). Basically, a *crease* is a line along which a fold takes place, a *vertex* is a point where creases converge, and panels are the regions bounded by creases. A *fold* is defined as a crease with an assigned fold angle, and it is divided by a *mountain*, convex to the plane (flat sheet of paper), and *valley*, concave to the plane. In a folding pattern, the Yoshizawa–Randlett notation system represents mountain folds as chain lines and valley folds as dashed lines [22]. The unit-cell of a six-crease waterbomb folding pattern is presented in Fig. 1.

Origami tessellation is a periodic arrangement of folding pattern unit-cells [8]. A cylindrical origami structure can be built from a waterbomb tessellation pattern, glueing its boundaries as presented in Fig. 2, which highlights each corresponding unit-cell.

The waterbomb folding pattern has been employed in several applications. The tessellation of the waterbomb base creates a deployable cylindrical origami structure with ability of changing its radius considerably. In this regard, Kuribayashi *et al.* [20] proposed a new type of stent graft (Fig. 3a) made of a single foldable NiTi foil. This biocompatible foil increases its radius by exploiting the shape memory effect using the body temperature. Lee *et al.* [23] presented an origami-inspired deformable wheel employed for autonomous robot using SMA actuators (Fig. 3b) that takes advantage of the wheel configuration to change force transmissibility and move through small gaps. In addition, path control can be performed through these configuration changes [13]. Although most of the research in origami-inspired robots has been focused on achieving mobility, origami-inspired grippers have also been successfully tested and prototyped. Li *et al.* [25] presented a vacuum-driven soft robotic gripper from an origami pattern that enables to produce significant grasp force under negative pneumatic pressure to be able to lift a large variety of objects (Fig. 3c). The waterbomb pattern has also been employed in energy harvesting applications due to its lightweight, flexibility, and self-rebounding properties. Pang *et al.* [32] presented a waterbomb origami-inspired triboelectric nanogenerator as a traffic monitoring system (Fig. 3.d).

3. Kinematics

The waterbomb unit-cell is modeled in this section considering a zero-thickness model with rigid panels, without deformations. Symmetry conditions are discussed highlighting the resulting models associated with each condition. The kinematic-based description can be carried out through an equivalent mechanism, as in robotics, where the creases are represented by revolute (or cylindrical) joints and the panels are represented by rigid links [3,15,28]. Specifically, the waterbomb pattern can be represented as a spherical mechanism where its movement is restricted to a sphere, with six links (panels) and six revolute joints (creases). Therefore, the rigid waterbomb pattern has *mobility* 3,

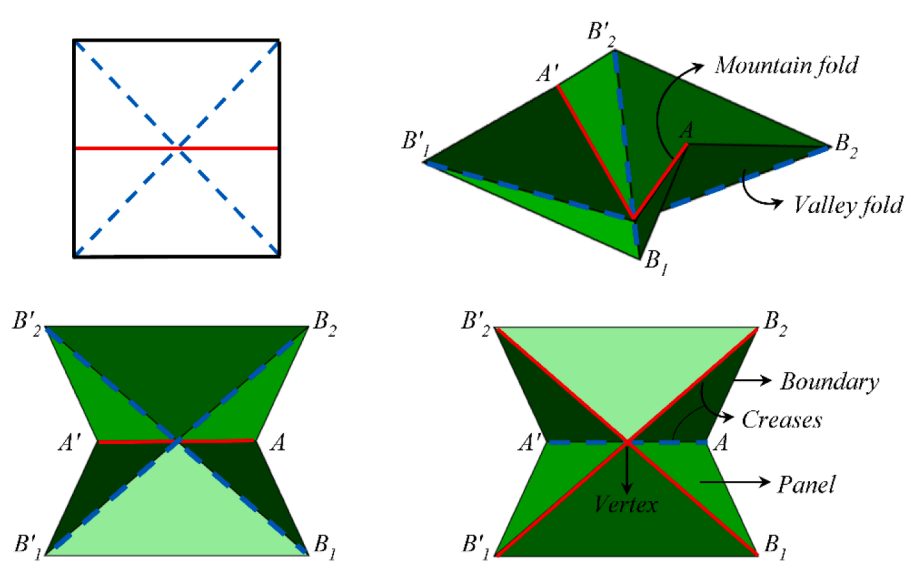

Fig. 1. The waterbomb folding pattern that consists of six creases and one vertex: (a) folding pattern in a flat paper; (b) folded pattern showing the creases in mountain folds (red lines) and valley folds (dashed blue lines). (c) top view and (d) bottom view of the folded paper.

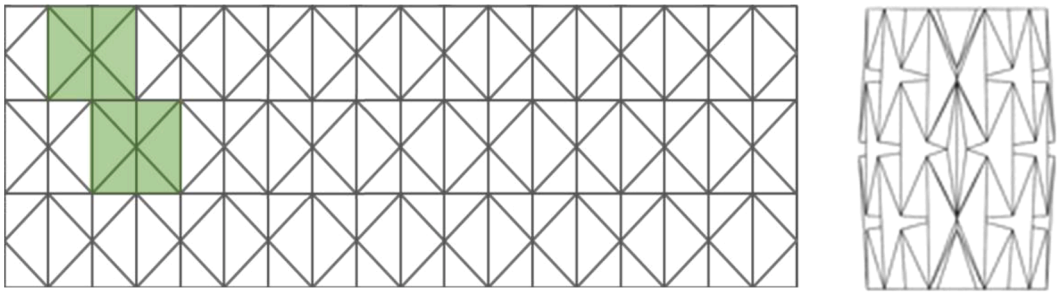

Fig. 2. Waterbomb pattern is tessellated in rows with a half unit-cell shift.

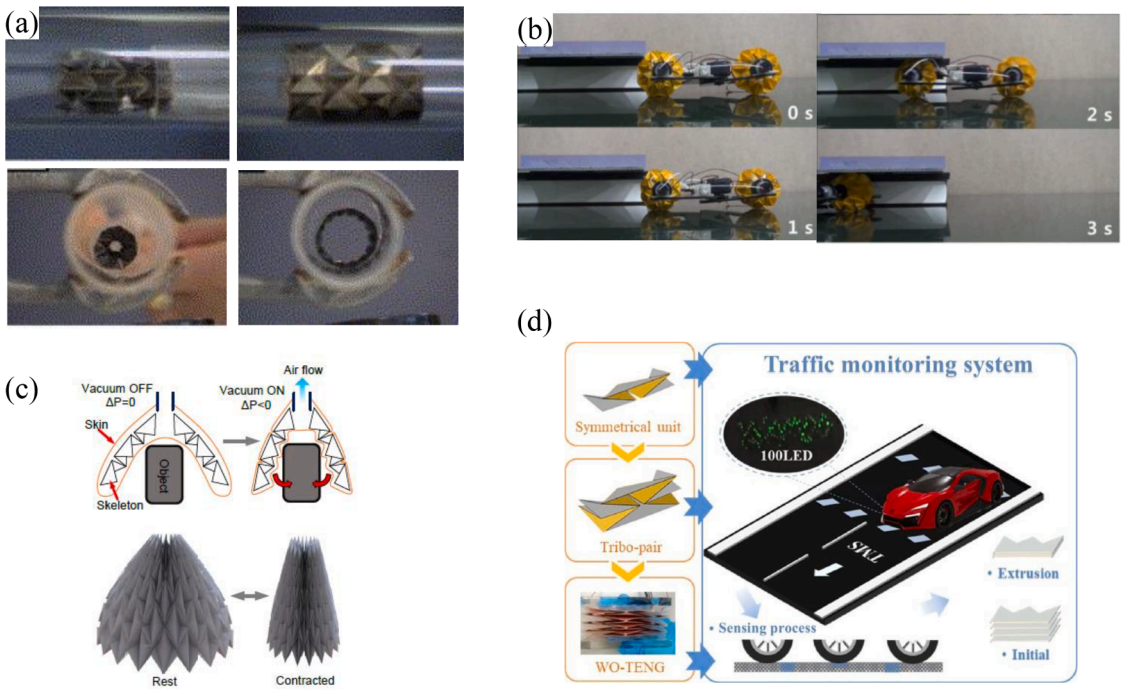

Fig. 3. Waterbomb applications. (a) An origami-inspired stent graft made of SMA that self-expands at temperatures above 319K [20]. (b) Origami-inspired deformable wheel that allows the robot to pass through slits that are smaller than the original wheel size. [23]. (c) The working principle of a vacuum-driven origami-inspired soft gripper [25]. (d) Waterbomb-origami inspired triboelectric nanogenerator for smart pavement-integrated traffic monitoring [32].

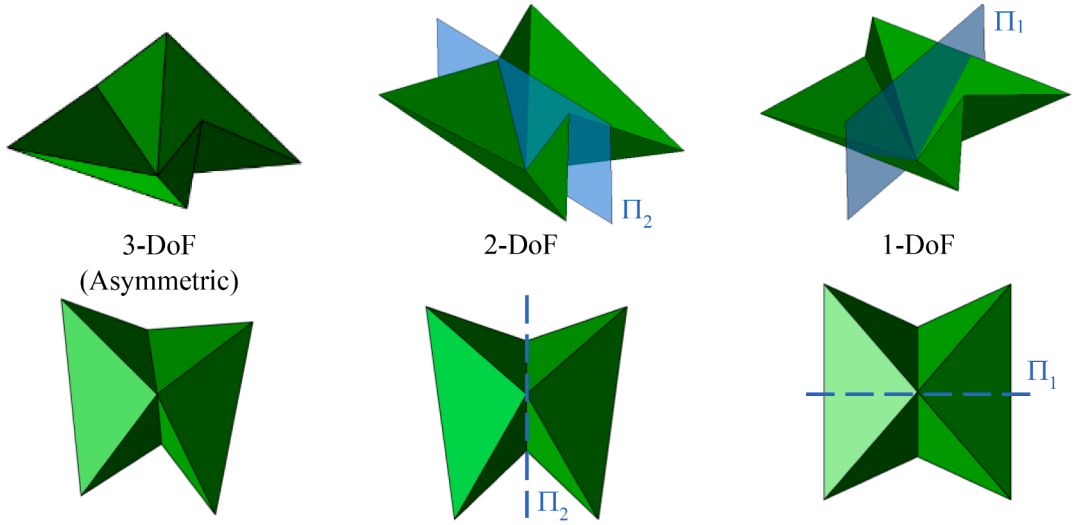

Fig. 4. A general waterbomb unit-cell is a 3-DoF system. Planes of symmetry can reduce it to a 2-DoF or even a 1-DoF system.

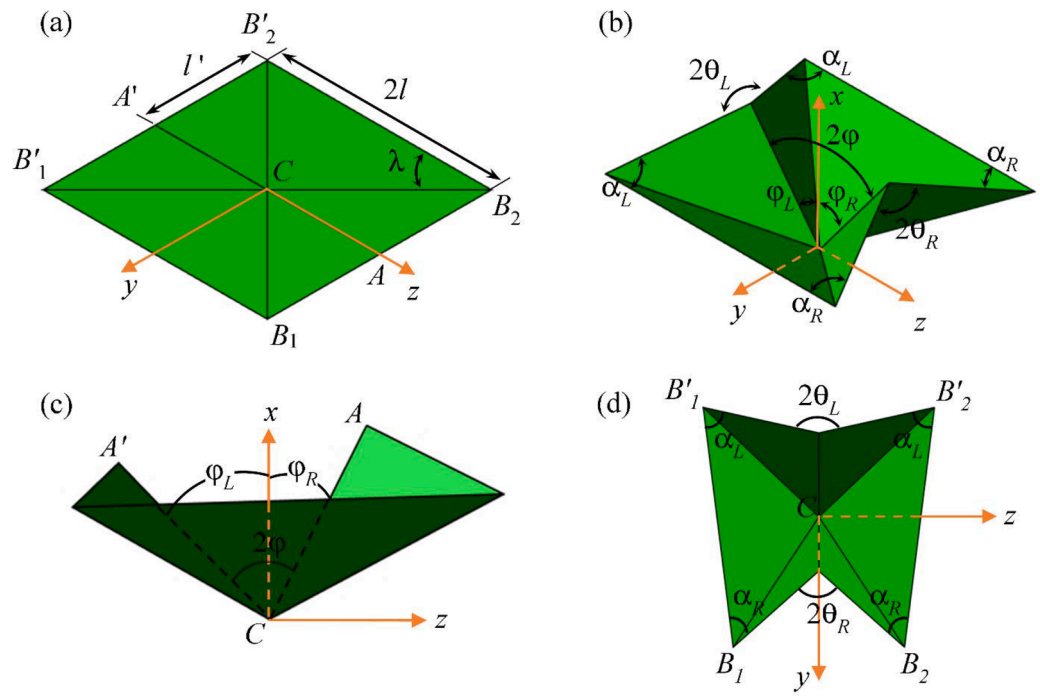

Fig. 5. Coordinate frame placement for the waterbomb unit-cell: (a) flat (unfolded) unit-cell; (b) folded unit-cell; (c) *xz*-view; (d) *yz*-view.

meaning that it is completely described by three angles [6,11,14].

Nevertheless, symmetry hypotheses are usually established, reducing the number of angles necessary to describe the deployment of the waterbomb unit-cell. Fonseca & Savi [14] presented two possible planes of symmetry: plane Π_2 that reduces the *mobility* to 2; and plane Π_1 that reduces the *mobility* to 1 (Fig. 4). Note that when the plane of symmetry Π_1 is considered, the plane of symmetry Π_2 is automatically considered due to geometric restrictions and rigid panel behavior. In other words, half of the waterbomb unit-cell can be analyzed in a 2-DoF model, and one-quarter of the waterbomb unit-cell in a 1-DoF model.

Another approach to deal with the origami kinematics is the direct geometric formulation (DGF), which is in focus henceforward. This approach develops straightforward mathematical relationships that allow a complete knowledge of the origami kinematics. Once again, symmetry assumptions are employed together with the rigid panel hypothesis [16,34].

The direct geometric approach starts by defining the coordinate frames. Fig. 5 shows the waterbomb pattern unit-cell considering side lengths l and l', and angle λ. The origin of the referential frame is placed at the central single vertex and the flat configuration is contained within *yz*-plane.

The general waterbomb unit-cell is a 3-DoF model, requiring the definition of three variables. Nevertheless, the assumption of a plane of symmetry Π_2 (Fig. 4) passing through AA' and normal to *yz*-plane allows the description of the waterbomb pattern with 2-DoF, for example, with variables θ_R and θ_L, as presented in Fig. 5. The assumption that $\theta = \theta_R = \theta_L$ is equivalent to assume the plane of symmetry Π_1, defining a 1-DoF model.

The coordinates of the vertices A, B_1 and $B_1^{'}$ (Fig. 5) are given by Equations (1) to (3). The vertex C is in the origin. The vertices A', B_2 and $B_2^{'}$ are mirrored of the vertices A, B_1 and $B_1^{'}$ by the plane of symmetry Π_2.

$$A = l\begin{bmatrix} \cos\varphi_R \\ 0 \\ \sin\varphi_R \end{bmatrix} \tag{1}$$

$$B_1 = l\begin{bmatrix} \cos\varphi_R - \tan\lambda\cos\theta_R\sin\varphi_R \\ \tan\lambda\sin\theta_R \\ \sin\varphi_R + \tan\lambda\cos\theta_R\cos\varphi_R \end{bmatrix} \tag{2}$$

$$B_1^{'} = l\begin{bmatrix} \cos\varphi_R - \tan\lambda\cos\theta_L\sin\varphi_R \\ \tan\lambda\sin\theta_L \\ -\sin\varphi_R - \tan\lambda\cos\theta_L\cos\varphi_R \end{bmatrix} \tag{3}$$

By considering a constraint equation associated with the geometric aspect of the rigid waterbomb origami model, $\overline{B_1B_1^{'}} = 2l$, it is possible to obtain the following trigonometric relation (the mathematical manipulations performed are explicit in Appendix A):

$$\begin{aligned} &\tan^2\lambda[\cos(2\varphi)\cos\theta_L\cos\theta_R - \sin\theta_L\sin\theta_R + 1] + \tan\lambda[\sin(2\varphi)(\cos\theta_L + \cos\theta_R)] \\ &- \cos(2\varphi) \\ &= 1 \end{aligned} \tag{4}$$

Equation (4) is then solved (as detailed in Appendix A) aiming to find $\varphi = \varphi(\theta_R,\ \theta_L)$:

$$\varphi = \begin{cases} \tan^{-1}\left(\dfrac{-(\cos\theta_R + \cos\theta_L) + \sqrt{4 - (\sin\theta_R + \sin\theta_L)^2 - (\tan\lambda)^2(\sin\theta_R - \sin\theta_L)^2}}{\tan\lambda(1 - \cos(\theta_R - \theta_L))}\right) & , \quad \theta_R \neq \theta_L \\ 2\tan^{-1}\left(\dfrac{1 - \tan\lambda\cos\theta_R}{1 + \tan\lambda\cos\theta_R}\right) & , \quad \theta_R = \theta_L \end{cases} \tag{5}$$

Eq. (5) shows the geometric coupling of the angle φ with the variables θ_R and θ_L. Because it is a 2-DoF system, any other angle in the unit-cell must have a relationship with these variables.

Angles α_L and α_R can also be written as a function of θ_R and θ_L. The angle α_R consists of the angle between the planes CAB_1 and $CB_1B'_1$ and the angle α_L is the angle between the planes $CA'B'_1$ and $CB_1B'_1$ (Fig. 5). Thus, the first step to find an expression for these angles is finding the normal vectors $\boldsymbol{n}$ to the planes. For instance, for the planes CAB_1 and $CB_1B'_1$: $\boldsymbol{n}_{CAB_1} = \overrightarrow{(B_1 - A)} \times \overrightarrow{(C - A)}$ and $\boldsymbol{n}_{CB_1B'_1} = \overrightarrow{(B_1 - C)} \times \overrightarrow{(C - B'_1)}$.

The angle α_R is the angle between the normal vectors:

$$\cos\alpha_R = \frac{\boldsymbol{n}_{CAB_1} \cdot \boldsymbol{n}_{CB_1B'_1}}{|\boldsymbol{n}_{CAB_1}| \left|\boldsymbol{n}_{CB_1B'_1}\right|} \tag{6}$$

The explicit expression for cos α_R is given by

$$\cos\alpha_R = \frac{\cos(2\varphi)\tan\lambda(1 + \cos\theta_L\cos\theta_R) + \sin(2\varphi)\left(\cos\theta_R - (\tan\lambda)^2\cos\theta_L\right) - \tan\lambda\sin\theta_L\sin\theta_R}{\sqrt{\Delta}} \tag{7}$$

where

$$\begin{aligned}\Delta \;=\; & (\cos2\varphi)^2(\tan\lambda)^2\cos\theta_L\cos\theta_R\left(2 - (\tan\lambda)^2\cos\theta_L\cos\theta_R\right) \\ & + (\sin2\varphi)^2\left(1 - (\tan\lambda)^2(\cos\theta_L + \cos\theta_R)^2\right) \\ & + (\cos2\varphi)(\tan\lambda)^2\sin\theta_L\sin\theta_R\left(2 - (\tan\lambda)^2\cos\theta_L\cos\theta_R\right) \\ & + (\sin2\varphi)2(\tan\lambda)^3(\sin\theta_L\sin\theta_R)(\cos\theta_L + \cos\theta_R) \\ & + (\cos2\varphi)(\sin2\varphi)2\tan\lambda(\cos\theta_L + \cos\theta_R)\left(1 - (\tan\lambda)^2\cos\theta_L\cos\theta_R\right) \\ & + (\tan\lambda)^2\left(2 + (\tan\lambda)^2\left[(\cos\theta_L)^2 + (\cos\theta_R)^2 - (\cos\theta_L)^2(\cos\theta_R)^2\right]\right)\end{aligned}$$

Analogous development is carried out for α_L :

$$\cos\alpha_L = \frac{\cos(2\varphi)\tan\lambda(1 + \cos\theta_L\cos\theta_R) + \sin(2\varphi)\left(\cos\theta_L - (\tan\lambda)^2\cos\theta_R\right) - \tan\lambda\sin\theta_L\sin\theta_R}{\sqrt{\Delta}} \tag{8}$$

The nonlinear characteristics of the origami kinematics can be observed by the relation among the angles φ, α_R, α_L and the variables θ_R and θ_L. Fig. 6 presents the level curves of each one of these angles with respect to θ_R and θ_L considering a square unit-cell ($\lambda = \pi/4$). These curves represent the nonlinear mechanical behavior of the deployment of the unit-cell.

4. Dynamics

Dynamical analysis considers a rigid origami model, with rigid panels, creases represented by linear torsional springs, and lumped masses on the vertices. Kinematics analysis developed by the direct geometric formulation is employed to describe the waterbomb unit-cell and Lagrange's equations are employed to obtain the equations of motion, neglecting gravitational effects. On this basis, a reduced-order dynamical model is built based on the origami unit-cell.

The rigid model assumes that the panels remain flat, without deformation during the deployment, and this characteristic is extended to the dynamical model. Besides, creases are represented by linear torsional springs and since there is a nonlinear relation between the angles (Fig. 6), the representative stiffness is essentially nonlinear. This geometric nonlinearity is responsible for the complex and nonlinear dynamics of the origami system.

In addition, lumped masses are assumed on the vertices, which means that the total mass of the unit-cell is equally distributed along the vertices. As a matter of fact, different mass distribution can be assumed based on different origami unit-cell deployment [24] considering a particle model, thin facet model and thick panel model. Nevertheless, results tend to be not sensitive to lumped masses model and distributed mass, especially in small scales. The lumped mass represents origami structures with light panels, being possible to represent the distribution by considering the mass located either at the vertices or at the panel centroid. The use of the mass at the vertices follows the idea that the creases have an important contribution for the mass of the structure. In other words, the vertices can be considered as points of interest with concentrated mass that must follow the movements given by the geometric relationship of the origami.

Following the Lagrange approach, the kinetic energy is derived from the velocity of the six lumped masses, by assuming that each vertex is assigned to an equal lumped mass (the central vertex is in the origin),

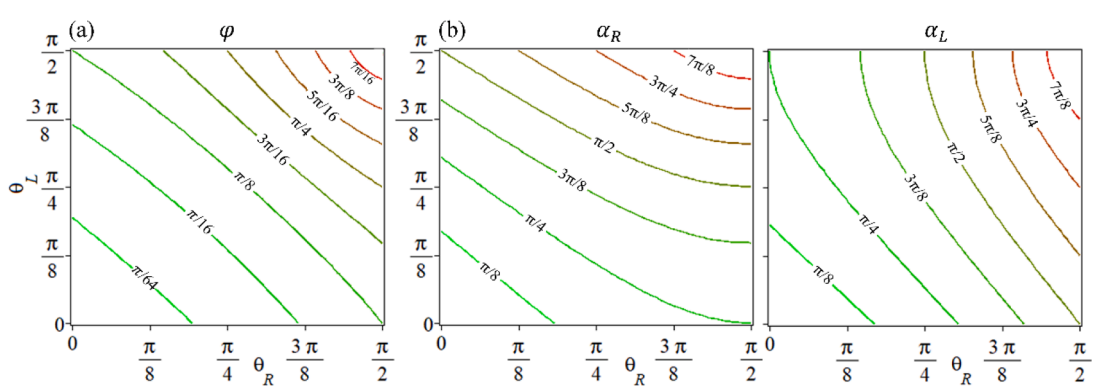

Fig. 6. Origami kinematics represented by angles of the 2-DoF square waterbomb model as a function of θ_R and θ_L: (a) φ. (b) α_R and α_L.

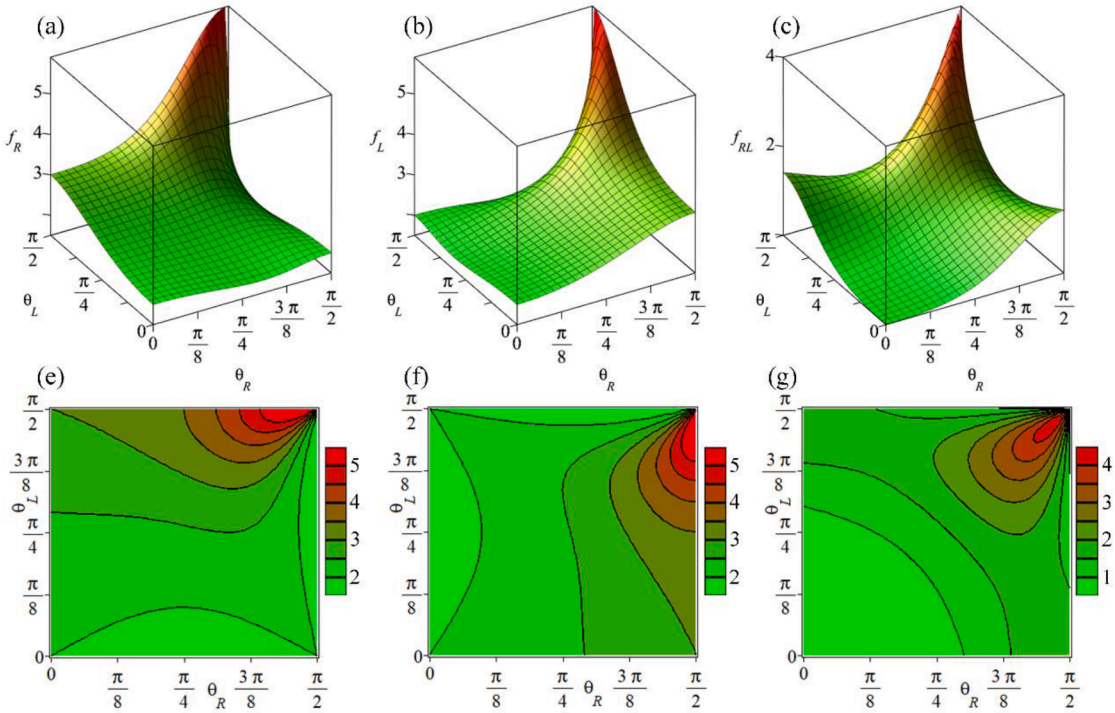

Fig. 7. Functions f_R, f_L and f_{RL} for the model with lumped masses. (a)-(c) Represent a 3D surface and (e)-(f) represent the respective contour map of the functions f_R, f_L and f_{RL}.

and each velocity is calculated from the time derivative of the vertex position. Therefore, by considering the plane of symmetry Π_2 (Fig. 4), the kinetic energy T is given by:

$$T = \frac{1}{2}m\left[2|\boldsymbol{v}_A|^2 + 2|\boldsymbol{v}_{B_1}|^2 + 2\left|\boldsymbol{v}_{B_1'}\right|^2\right] \tag{9}$$

where m is the lumped mass and $\boldsymbol{v}$ is the velocity of the assigned vertex.

By considering the position of the vertices, Eq. (1) to Eq. (3), and calculating their time derivative, the velocities $\boldsymbol{v}_A$, $\boldsymbol{v}_{B_1}$ and $\boldsymbol{v}_{B_1'}$ of the vertices A, B_1 and B_1' are described as follows where it is important to remember that $\varphi = \varphi(\theta_R, \theta_L)$,

$$\boldsymbol{v}_A = l\begin{bmatrix} -(\sin\varphi_R)\dot{\varphi}_R \\ 0 \\ (\cos\varphi_R)\dot{\varphi}_R \end{bmatrix} \tag{10}$$

$$\boldsymbol{v}_{B_1} = l\begin{bmatrix} -(\sin\varphi_R + \tan\lambda\cos\varphi_R\cos\theta_R)\dot{\varphi}_R + (\tan\lambda\sin\varphi_R\sin\theta_R)\dot{\theta}_R \\ (\tan\lambda\cos\theta_R)\dot{\theta}_R \\ (\cos\varphi_R - \tan\lambda\sin\varphi_R\cos\theta_R)\dot{\varphi}_R - (\tan\lambda\cos\varphi_R\sin\theta_R)\dot{\theta}_R \end{bmatrix} \tag{11}$$

$$\boldsymbol{v}_{B_1'} = l\begin{bmatrix} -(\sin\varphi_R + \tan\lambda\cos\varphi_R\cos\theta_L)\dot{\varphi}_R + (\tan\lambda\sin\varphi_R\sin\theta_L)\dot{\theta}_L \\ (\tan\lambda\cos\theta_L)\dot{\theta}_L \\ -(\cos\varphi_R - \tan\lambda\sin\varphi_R\cos\theta_L)\dot{\varphi}_R + (\tan\lambda\cos\varphi_R\sin\theta_L)\dot{\theta}_L \end{bmatrix} \tag{12}$$

Since the values of φ_R and φ_L are known, and therefore the value of 2φ, it is possible to determine a coordinate system where $\varphi = \varphi_R = \varphi_L$

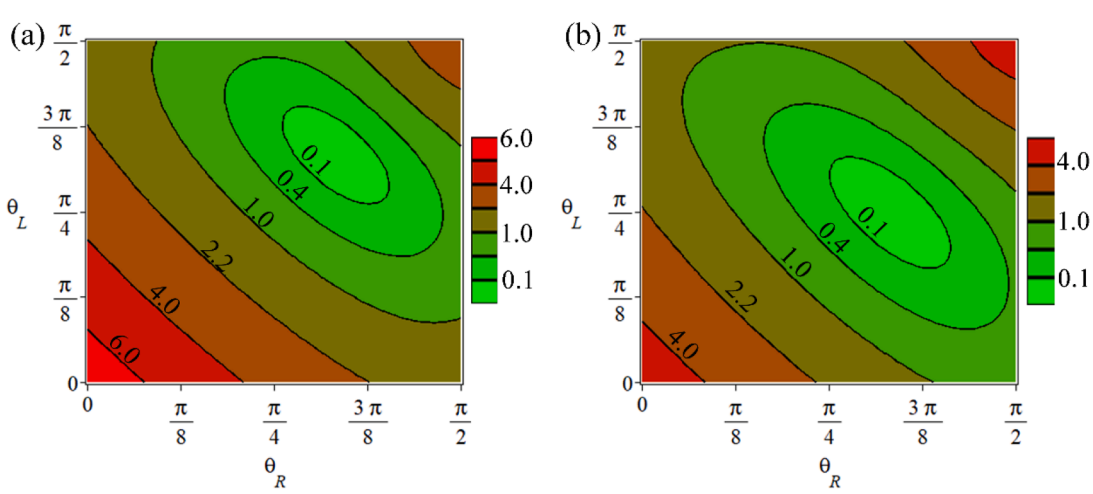

Fig. 8. Contour map of the potential energy of the 2-DoF waterbomb unit-cell model with torsional springs in the creases ($\bar{k}_\theta = \bar{k}_\alpha$). (a) $\theta_{L0} = \theta_{R0} = \pi/3$. (b) $\theta_{L0} = \pi/4$ and $\theta_{R0} = \pi/3$.

without loss of generality and even without changing the values of θ_R and θ_L, which are intrinsic to the geometry of the unit-cell.

By substituting Eq. (10) to (12) in equation Eq. (9), it is possible to rewrite the kinetic energy T as follows:

$$T = \frac{1}{2} m l^2 \left(\dot{\theta}_R^2 f_R + \dot{\theta}_L^2 f_L + \dot{\theta}_R \dot{\theta}_L f_{RL} \right) \tag{13}$$

where $f_L = f_L(\theta_R, \theta_L)$, $f_R = f_R(\theta_R, \theta_L)$ and $f_{RL} = f_{RL}(\theta_R, \theta_L)$ are nonlinear functions with the form presented as follows and represented in Fig. 7.

$$f_R = 6\left(\frac{d\varphi}{d\theta_R}\right)^2 - 4\tan\lambda \frac{d\varphi}{d\theta_R}\sin\theta_R + 2\tan^2\lambda\left[\left(\frac{d\varphi}{d\theta_R}\right)^2\left(\cos^2\theta_L + \cos^2\theta_R\right) + 1\right] \tag{14}$$

$$f_L = 6\left(\frac{d\varphi}{d\theta_L}\right)^2 - 4\tan\lambda \frac{d\varphi}{d\theta_L}\sin\theta_L + 2\tan^2\lambda\left[\left(\frac{d\varphi}{d\theta_L}\right)^2\left(\cos^2\theta_L + \cos^2\theta_R\right) + 1\right] \tag{15}$$

$$f_{RL} = 12\frac{d\varphi}{d\theta_L}\frac{d\varphi}{d\theta_R} - 4\tan\lambda\left(\frac{d\varphi}{d\theta_L}\sin\theta_R + \frac{d\varphi}{d\theta_R}\sin\theta_L\right) + 4\tan^2\lambda\frac{d\varphi}{d\theta_L}\frac{d\varphi}{d\theta_R}\left[\left(\frac{d\varphi}{d\theta_L}\right)^2\left(\cos^2\theta_L + \cos^2\theta_R\right)\right] \tag{16}$$

The elastic potential energy U is defined as follows, based on the torsional springs associated with the six creases:

$$U = \frac{1}{2}\left[\bar{k}_\theta\left(2\theta_L - 2\theta_{L_0}\right)^2 + \bar{k}_\theta\left(2\theta_R - 2\theta_{R_0}\right)^2 + 2\bar{k}_\alpha\left(\alpha_L - \alpha_{L_0}\right)^2 + 2\bar{k}_\alpha\left(\alpha_R - \alpha_{R_0}\right)^2\right] + U_{lim} \tag{17}$$

where $\bar{k}_\theta$ and $\bar{k}_\alpha$ are torsional stiffness, θ_{L0}, θ_{R0}, α_{L0} and α_{R0} are the angles corresponding to the stress-free stable configuration and U_{lim} represents a potential energy associated with a physical limits due to panels interactions of the origami.

It is highlighted that α_L and α_R are functions of θ_L and θ_R, while α_{L0} and α_{R0} are functions of θ_{L0} and θ_{R0} which correspond to angles of the equilibrium state. Fig. 8 presents the potential energy as a contour map for $\bar{k}_\theta = \bar{k}_\alpha$ and different values of θ_{L0} and θ_{R0}.

By considering the Lagrangian $\mathscr{L} = T - U$ where θ_R and θ_L are the generalized coordinates; $\bar{Q}_R$ and $\bar{Q}_L$ are the external generalized forces, it is written the Lagrange's equations:

$$\begin{cases} \dfrac{d}{dt}\left(\dfrac{d\mathscr{L}}{d\dot{\theta}_R}\right) - \dfrac{d\mathscr{L}}{d\theta_R} = \bar{Q}_R \\ \dfrac{d}{dt}\left(\dfrac{d\mathscr{L}}{d\dot{\theta}_L}\right) - \dfrac{d\mathscr{L}}{d\theta_L} = \bar{Q}_L \end{cases} \tag{18}$$

By using the kinetic and potential energy equations, Eq. (13) and Eq. (17), into the Lagrange's equation, the equations of motion are obtained:

$$\begin{cases} ml^2\left(2f_R\ddot{\theta}_R + f_{RL}\ddot{\theta}_L + g_R\dot{\theta}_R^2 + h_L\dot{\theta}_L^2 + g_{RL}\dot{\theta}_R\dot{\theta}_L\right) + \bar{M}_R = \bar{Q}_R \\ ml^2\left(2f_L\ddot{\theta}_L + f_{RL}\ddot{\theta}_R + g_L\dot{\theta}_L^2 + h_R\dot{\theta}_R^2 + g_{LR}\dot{\theta}_R\dot{\theta}_L\right) + \bar{M}_L = \bar{Q}_L \end{cases} \tag{19}$$

Where the dots $(\dot{})$ represents time derivative; $g_R = 2\frac{df_R}{dt} + \frac{df_R}{d\theta_R}$, $h_L = \frac{df_{RL}}{dt} + \frac{df_L}{d\theta_R}$ and $g_{RL} = 2\frac{df_R}{dt} + \frac{df_{RL}}{dt} + \frac{df_{RL}}{d\theta_R}$ are nonlinear functions (which are similar to g_L, h_R and g_{LR}); $\bar{M}_R = \frac{dU}{d\theta_R}$ and $\bar{M}_L = \frac{dU}{d\theta_L}$ are the nonlinear torques related to the torsional springs associated with the creases.

Physical limits are established by a proper definition of the domain, which is done in order to avoid material interpenetration due to panel intersections. Therefore, the description of the waterbomb unit-cell considers that the minimum deployment angles are θ_R and θ_L equal to zero, where all the panels are in the same plane and in contact with each other. The maximum angle is $\pi/2$, meaning that the panels are flat. This physical limitation is represented by extra terms $\bar{M}_{lim_R}$ and $\bar{M}_{\mathrm{lim}L}$, Eq. (20), which are derived from U_{lim}, that are added to the equations considering a high stiffness $\bar{k}_{lim}$. Fig. 9 presents some shapes of the waterbomb unit-cell, highlighting these limits.

$$\bar{M}_{lim_R} = \begin{cases} \bar{k}_{lim}\theta_R & , \quad \theta_R \le 0 \\ \bar{k}_{lim}\left(\theta_R - \dfrac{\pi}{2}\right) & , \quad \theta_R \ge \dfrac{\pi}{2} \\ 0 & , \quad \text{otherwise} \end{cases} \tag{20.a}$$

$$M_{lim_L} = \begin{cases} \bar{k}_{lim}\theta_L & , \quad \theta_L < 0 \\ \bar{k}_{lim}\left(\theta_L - \dfrac{\pi}{2}\right) & , \quad \theta_L > \dfrac{\pi}{2} \\ 0 & , \quad \text{otherwise} \end{cases} \tag{20.b}$$

Aiming to write the equations of motion in a dimensionless form, a dimensionless time $\tau = \omega t$ is assumed, where ω is a reference frequency. Besides, linear viscous dissipation of the form $-\xi\dot{\theta}_R$ and $-\xi\dot{\theta}_L$ are incorporated, which is added in the right side of the equations Eq. (19) as a nonconservative generalized force. In this regard, the following dimensionless system of first-order differential equations is written:

$$\begin{cases} \theta_R^* = \theta_{v_R} \\ \theta_R^{**} = f_1\theta_R^{*2} + f_2\theta_L^{*2} + f_3\,\theta_R^*\theta_L^* + \xi\left(f_4\theta_R^* + f_5\theta_L^*\right) + M_R + Q_R \\ \theta_L^* = \theta_{v_L} \\ \theta_L^{**} = g_1\theta_L^{*2} + g_2\theta_R^{*2} + g_3\theta_R^*\theta_L^* + \xi\left(g_4\theta_L^* + g_5\theta_R^*\right) + M_L + Q_L \end{cases} \tag{21}$$

Table 1
Parameters of the 2-DoF model of the waterbomb unit-cell.

m (kg)	ξ (N m s/rad)	l (m)	$\bar{k}_\theta = \bar{k}_\alpha$ (N m/rad)
50×10^{-3}	1×10^{-4}	60×10^{-3}	1×10^{-4}

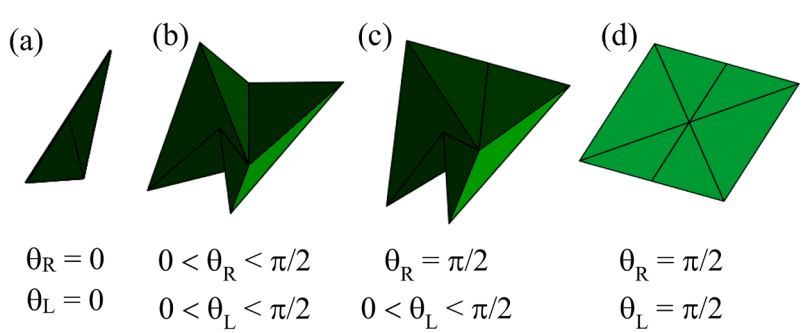

Fig. 9. Different limit shapes of the waterbomb unit-cell. (a) fully folded; (b) unfolded; (c) folded at the limit angle of θ_R; (d) fully unfolded (flat).

where $(\ )^* = d()/d\tau$ and, therefore, $\dot{\theta}_R = \theta_R^* \omega$ and $\ddot{\theta}_R = \theta_R^{**} \omega^2$ (and similar to θ_L). The dimensionless nonlinear functions are given by:

$$f_1 = \frac{-2f_L g_R + f_{RL} h_R}{4f_R f_L - f_{RL}^2} \tag{22.a}$$

$$f_2 = \frac{-2f_L h_L + f_{RL} g_L}{4f_R f_L - f_{RL}^2} \tag{22.b}$$

$$f_3 = \frac{-2f_L g_{RL} + f_{RL} g_{LR}}{4f_R f_L - f_{RL}^2} \tag{22.c}$$

$$f_4 = \frac{-2f_L}{ml^2\left(4f_R f_L - f_{RL}^2\right)} \tag{22.d}$$

$$f_5 = \frac{f_{RL}}{ml^2\left(4f_R f_L - f_{RL}^2\right)} \tag{22.e}$$

$$M_R = \frac{-2f_L(\bar{M}_R + \bar{M}_{lim_R}) + f_{RL}(\bar{M}_L + \bar{M}_{lim_L})}{ml^2\left(4f_R f_L - f_{RL}^2\right)} \tag{22.f}$$

$$Q_R = \frac{2f_L \bar{Q}_R - f_{RL} \bar{Q}_L}{ml^2\left(4f_R f_L - f_{RL}^2\right)} \tag{22.g}$$

5. Numerical Simulations

This section is dedicated to numerical simulations of the waterbomb unit-cell considering different symmetry conditions. The equations of motion, Eq. (21), are integrated employing the fourth order Runge-Kutta method implemented in Fortran. Time steps are chosen after a convergence analysis and values less than 5×10^{-3} present good results. The frequency $\omega = \sqrt{\frac{\bar{k}_\theta}{ml^2}}$ is adopted as reference and simulations are performed to ensure that transients have elapsed, and a steady-state solution is attained. A harmonic external stimulus is considered in the form of a torque $\bar{Q}_R = \bar{\mu}\sin\Omega t$ in the crease related to the angle θ_R; similar condition is imposed by torque $\bar{Q}_L$ in the crease related to the angle θ_L. Parameters presented in Table 1 are considered for all the simulations.

Three different symmetry conditions are analyzed considering the following cases (Fig. 10): Case 1, symmetric waterbomb unit-cell ($\theta_{R0} = \theta_{L0}$) subjected to symmetric stimuli represented by torques ($Q_R = Q_L$) applied in the generalized coordinates θ_R and θ_L, equivalent to a symmetric 1-DoF system; Case 2, symmetric waterbomb unit-cell ($\theta_{R0} = \theta_{L0}$), subjected to asymmetric external stimuli represented by torque applied in θ_R, which means that $Q_L = 0$, equivalent to an asymmetric 2-DoF system; and Case 3, plane-symmetric waterbomb ($\theta_{R0} \neq \theta_{L0}$) subjected to symmetric stimuli represented by torques applied in θ_R and θ_L ($Q_R = Q_L$), equivalent to an asymmetric 2-DoF system.

A general comprehension of the system dynamics is provided by limit configuration maps and bifurcation diagrams. Fig. 11 presents limit configuration representative map for different amplitude, $\bar{\mu}$, and frequency, $\bar{\Omega}$, of the external stimuli. The green color means situations where the physical limits are not reached while the red color means that at least one physical limit, 0 or $\pi/2$, is reached. Fig. 11a considers $\theta_{R0} = \theta_{L0} = 60^\circ$ and $Q_R = Q_L$ (Case 1, Fig. 10), Fig. 11b considers $\theta_{R0} = \theta_{L0} = 60^\circ$ and $Q_L = 0$ (Case 2, Fig. 10) and Fig. 11c considers $\theta_{R0} = 45^\circ$ and $\theta_{L0} = 60^\circ$ (Case 3, Fig. 10). It is noticeable that the system, in any of the three cases, oscillates without reaching the physical limits for frequencies from 2.0 to 2.1 for all forcing amplitudes considered. This band is broadened from 1.7 to 2.1 in the asymmetric 2-DoF system with different initial angles (Case 3) and it is more broadened in the symmetric 1-DoF system (Case 1), from 1.3 to 2.1. These maps illustrate the differences of the dynamical behaviors considering the whole symmetric (1-DoF system) and the asymmetric (2-DoF system) models, further the differences in the symmetry conditions (Cases 2 and 3). Therefore, it should be pointed out the notable differences in the dynamical responses accordingly to the symmetry assumption.

These results highlight the importance of the model choice and, in addition, defines symmetry conditions that can be chosen according to the application using either initial configuration or external stimulus. This motivates the design of programmed unit-cell in order to obtain a desired result. For example, energy harvesting applications (Fig. 3d) seeks high amplitudes and therefore, the unit-cell can be programmed to operate in an advantageous specific zone. On the other hand, an origami structure composed by a tessellation of the unit-cell (Fig. 2) usually presents a plane-symmetric unit-cell configuration (Fig. 3c) due to the interaction to adjacent unit-cells. Besides, the physical limits constitute a relevant source of nonlinearity, being important to characterize the dynamical behavior.

A global comprehension of the system dynamics is now in focus by

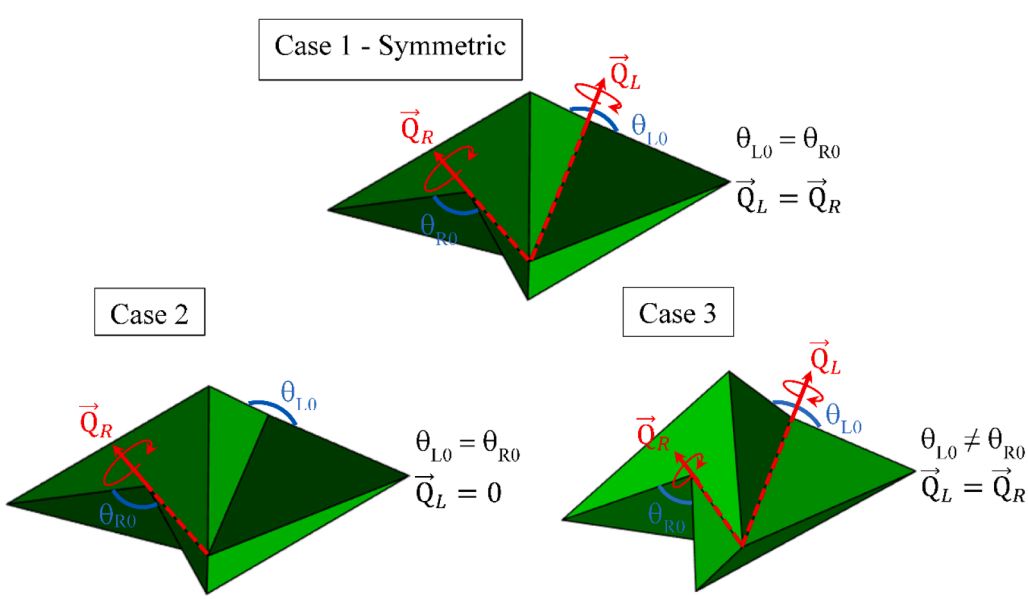

Fig. 10. Different symmetry conditions of the origami unit-cell. Case 1: symmetric waterbomb unit-cell subjected to symmetric torques applied in both creases (1-DoF system). Case 2: symmetric waterbomb unit-cell subjected to an asymmetric torque applied in one crease (related to θ_R) (2-DoF system). Case 3: plane-symmetric waterbomb unit-cell with symmetric torques applied in both creases (related to θ_R and θ_L) (2-DoF system).

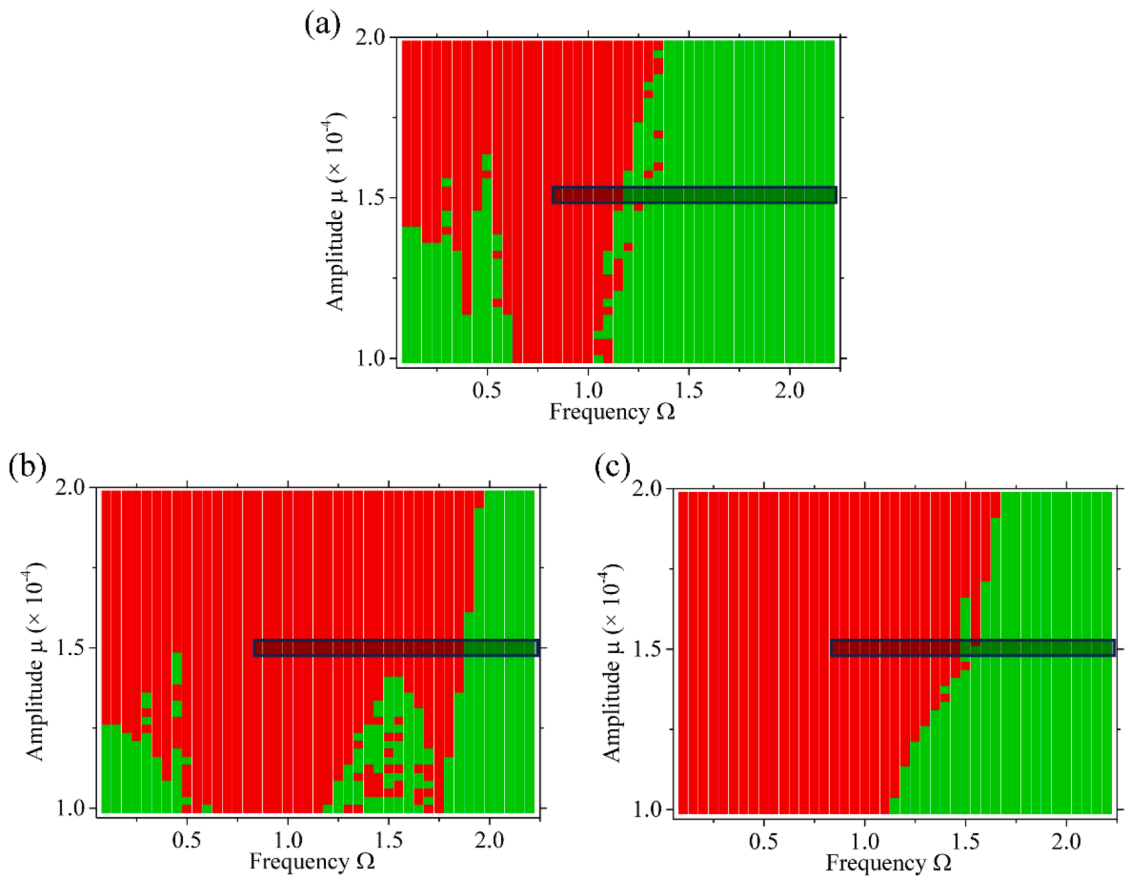

Fig. 11. Representative map of the waterbomb unit-cell with 2-DoF. Green points mean that physical limits are not reached and the red point mean that physical limits are reached. (a) Case 1: symmetric 1-DoF unit-cell subjected to symmetric stimuli. Case 2: symmetric 2-DoF unit-cell subjected to asymmetric stimuli. Case 3: plane-symmetric 2-DoF unit-cell subjected to symmetric stimuli.

the perspective of bifurcation diagrams that are built from the stroboscopically sampled angular displacement θ_R against the slow quasi-static variation of the frequency $\bar{\Omega}$ of the external stimulus. Bifurcation diagrams varying the frequency $\bar{\Omega}$ from 0.8 to 2.2 and a constant forcing amplitude $\bar{\mu} = 1.5\times10^{-4}$ Nm is shown in Fig. 12 considering the three symmetry condition cases. These cases are highlighted in the representative map (green and red) of Fig. 11, and the same colors are employed to identify the situation when the limit cases are reached. In general, when the physical limits are not reached (green), a periodic response is observed. On the other hand, when the physical limits are reached (red), a rich dynamical behavior is observed, with high periodicity and chaotic-like responses. Fig. 12a presents predominantly a periodic behavior. It is noticeable from Fig. 12b that a periodic behavior occurs until close to $\bar{\Omega} = 1.57$, where a chaotic-like response takes place until $\bar{\Omega} = 1.90$. Afterward, a bifurcation is noted from chaotic to a periodic response. Fig. 12c presents this chaotic-like zone from $\bar{\Omega} = 1.26$ to $\bar{\Omega} = 1.33$, and the system response becomes predominantly periodic after this zone. A chaotic-like behavior is noticeable close to $\bar{\Omega} = 1.52$, but without reach the system limits.

The comparison of the bifurcation diagrams of the three symmetry condition cases shows that the symmetric 1-DoF unit-cell (Case 1) does not present a chaotic behavior in the analyzed frequency range; the symmetric 2-DoF unit-cell (Case 2) presents a window of chaotic-like behavior. Such window is shortened when considering the plane-symmetric 2-DoF unit-cell (Case 3). These results highlight the different dynamical behavior of the system accordingly to the symmetry conditions.

It is noticeable that for $\bar{\Omega} = 0.80$, a high periodic response is observed for Case 1, but period-1 responses for both Case 2 and Case 3. For $\bar{\Omega} = 1.30$, a period-1 response occurs for Case 1 and Case 2, while a chaotic-like response is observed for Case 3. It should be pointed out that Case 3 is the only condition where a chaotic-like behavior is observed in the green zone, where limit configuration is not reached. Besides, all the cases present a period-1 behavior for high frequencies, upward $\bar{\Omega} = 2.00$.

Specific responses are now treated in the sequel considering each one of the symmetry conditions. Initially, Case 1 is of concern, considering situations identified by A_1 to D_1 in the bifurcation diagram (Fig. 12). Phase spaces (displacement-velocity orbits) of these cases are presented in Fig. 13. At the left side of the bifurcation diagram, A_1 ($\bar{\Omega} = 0.80$) has a high periodicity response, represented in Fig. 13a. The other solutions are all periodic, period-2 in B_1 ($\bar{\Omega} = 0.85$) and period-1 in C_1 ($\bar{\Omega} = 1.00$) and D_1 ($\bar{\Omega} = 1.40$). A change of the response amplitude is also noticeable for higher frequencies, as pointed out by the Fig. 13d.

The analysis of phase spaces corresponding to Case 2, identified by A_2 to D_2 in the bifurcation diagram, are presented in Fig. 14. Period-2 response is observed in A_2 ($\bar{\Omega} = 0.85$), while a period-1 response occurs in B_2 ($\bar{\Omega} = 1.40$). A chaotic response is observed in C_2 ($\bar{\Omega} = 1.80$). In all these cases, the system oscillates up to the physical limits, that is, the unit-cell fold and unfold completely. In D_2 ($\bar{\Omega} = 1.92$), a periodic response takes place without reaching the physical limits.

Case 3 is now of concern in Fig. 15 that shows phase spaces corresponding to the parameters identified from A_3 to D_3 on the bifurcation diagram. Period-1 responses are observed in A_3 ($\bar{\Omega} = 1.00$) and D_3 ($\bar{\Omega} = 1.80$) while chaotic responses are observed in B_3 ($\bar{\Omega} = 1.30$) and C_3 ($\bar{\Omega} = 1.52$). In A_3 and B_3, the physical limits are reached while the cases C_3 and D_3 do not reach these limits.

A comparison of the dynamical behavior of each of the three cases for

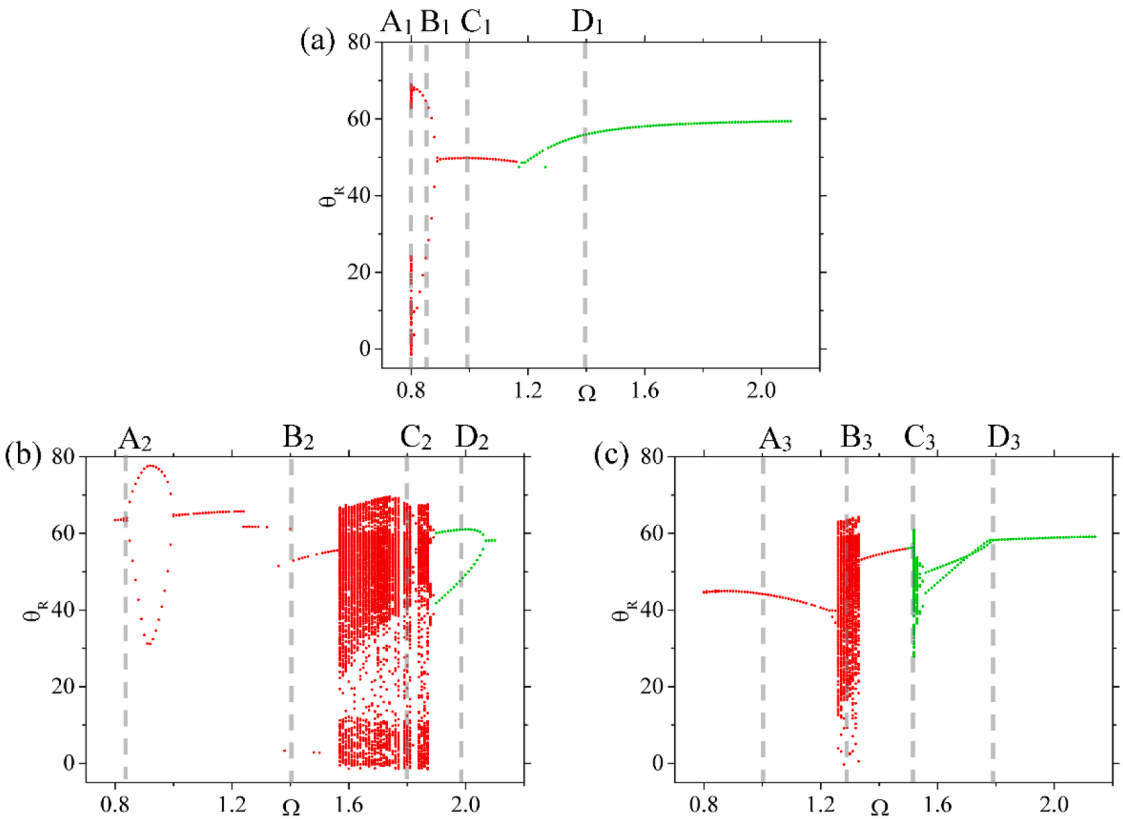

Fig. 12. Bifurcation diagram varying $\bar{\Omega}$ ($\bar{\mu} = 1.5\times10^{-4}$ Nm). (a) Case 1: symmetric 1-DoF unit-cell. (b) Case 2: symmetric 2-DoF unit-cell subjected to asymmetric stimuli. (c) Case 3: plane-symmetric 2-DoF unit-cell with symmetric stimuli.

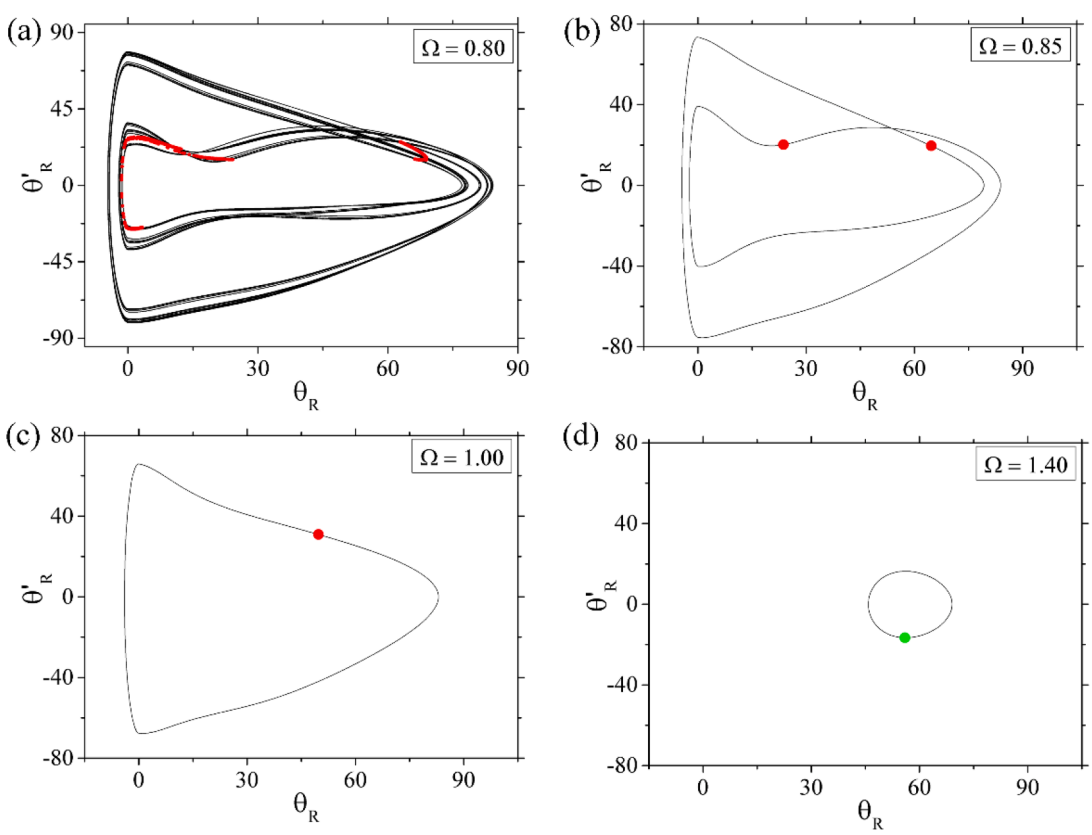

Fig. 13. Case 1 – symmetric 1-DoF unit-cell: phase spaces of the points A_1 to D_1 indicated in the bifurcation diagram.

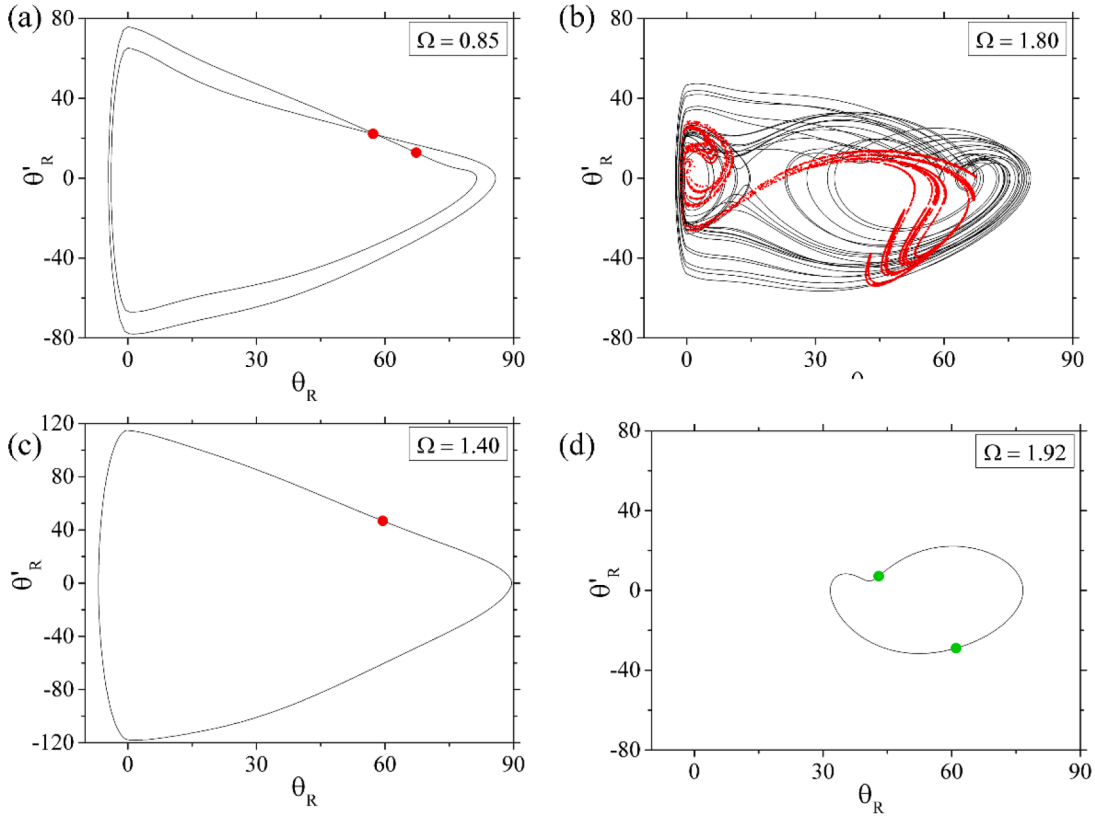

Fig. 14. Case 2 – symmetric 2-DoF unit-cell: phase spaces of the points A_2 to D_2 indicated in the bifurcation diagram (Case 2).

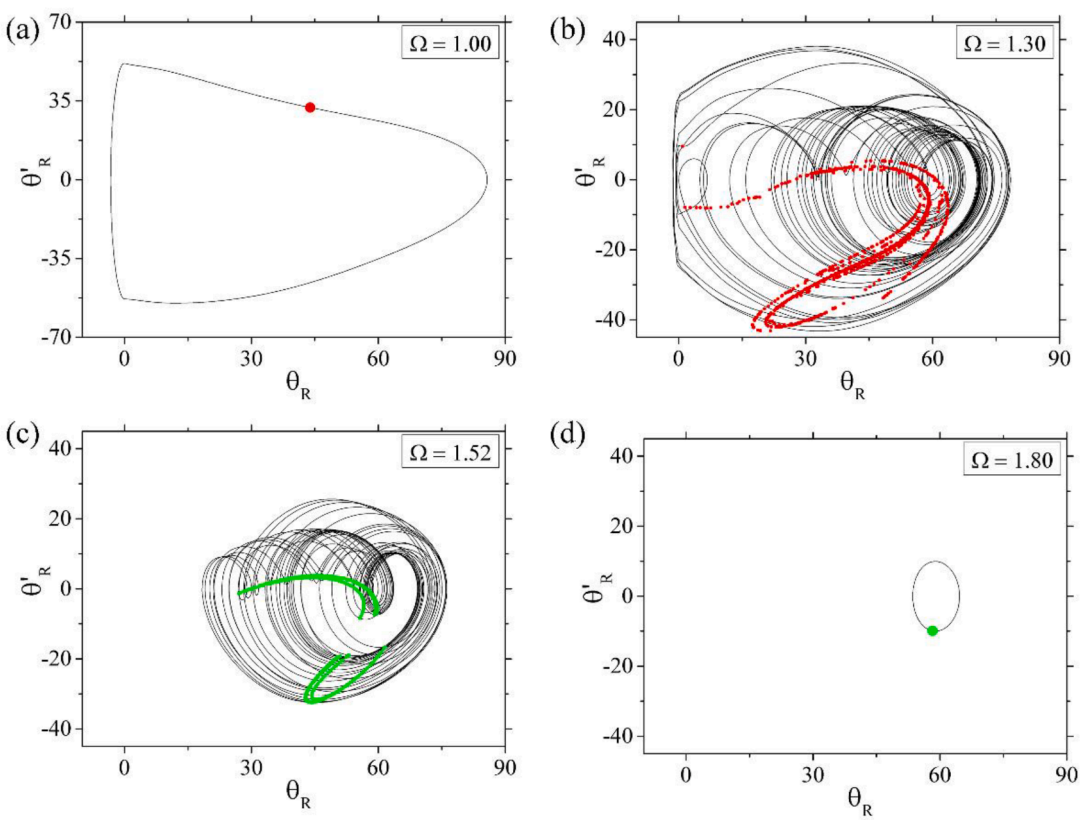

Fig. 15. Case 3 - plane-symmetric 2-DoF unit-cell: phase spaces of the points A_3 to B_3 indicated in the bifurcation diagram (Case 3).

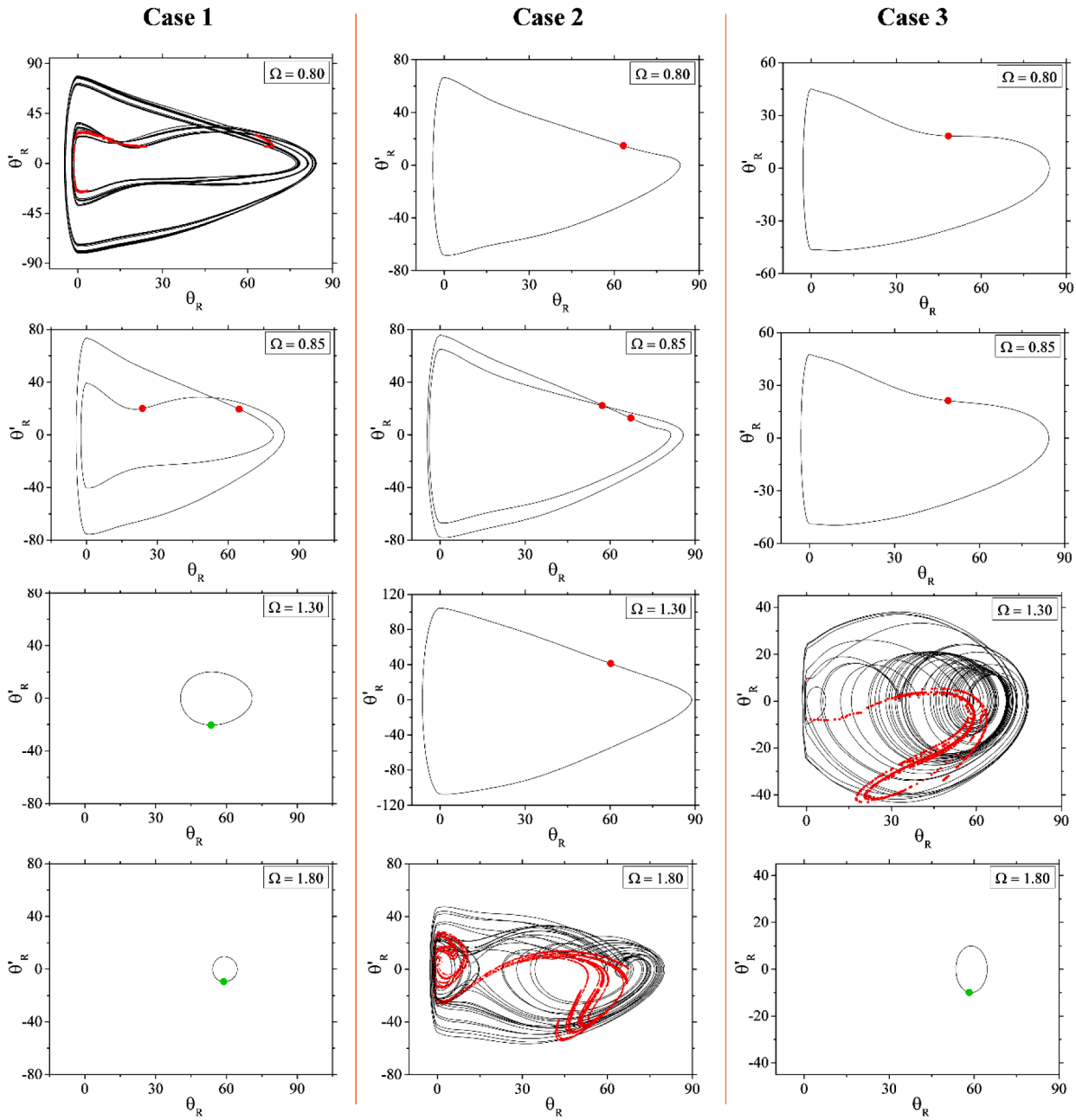

Fig. 16. Comparison of the phase spaces of Cases 1, 2 and 3 under the same frequencies. From top to bottom, the frequencies $\bar{\Omega}$ are 0.80, 0.85, 1.30 and 1.80.

the same frequency and forcing amplitudes is now of concern (Fig. 16). For $\bar{\Omega} = 0.80$, the 1-DoF unit-cell (Case 1) presents a high periodic response while the 2-DoF unit-cell presents a period-1 response. On the other hand, for $\bar{\Omega} = 0.85$, both the symmetric 1-DoF and symmetric 2-DoF unit-cell show period-2 response, whereas the plane-symmetric 2-DoF unit-cell (Case 3) shows a period-1 response. Notable changes are observed for $\bar{\Omega} = 1.30$. The symmetric 1-DoF and symmetric 2-DoF unit-cell present a period-1 response, but the amplitude of the response of the 2-DoF unit-cell is considerably higher. Moreover, the plane-symmetric unit-cell (Case 3) presents a chaotic response. This drastic difference is also noted for $\bar{\Omega} = 1.80$, where the symmetric 1-DoF and plane-symmetric unit-cell present a period-1 response while the symmetric 2-DoF unit-cell (Case 2) presents a chaotic response. On this basis, origami system presents a rich dynamics with distinct possibilities related to symmetry conditions. This analysis highlights the importance of a proper modeling of the nonlinear origami system.

6. Conclusions

This work deals with the nonlinear dynamics of a waterbomb unit-cell modeled by different symmetry conditions. Although waterbomb origami systems have several engineering applications, their nonlinear dynamics is still not completely explored in the literature. A dynamical model is built from the kinematics of the folding pattern, leading to different models defined by 1-DoF and 2-DoF models. A reduced-order dynamical system is built by assuming lumped masses on the vertices and torsional linear springs on the creases. Nonlinear dynamical analysis is established considering different symmetry conditions and external stimuli. Basically, three different cases are treated: Case 1, symmetric unit-cell subjected to symmetric stimuli - symmetric 1-DoF system; Case 2, symmetric unit-cell subjected to asymmetric external stimuli - asymmetric 2-DoF system; and Case 3, plane-symmetric unit-cell subjected to symmetric external stimuli - asymmetric 2-DoF system.

A proper understanding of the global dynamical behavior is provided by physical limit maps and bifurcation diagrams built for different symmetry conditions. The analysis of physical limits shows their importance due to the new source of nonlinearity. Results show a significant difference among the three symmetry conditions treated. For instance, a symmetric waterbomb unit-cell under asymmetric stimuli and a plane-symmetric waterbomb under symmetric stimuli present huge qualitative differences. Both cases present complex behaviors especially when the physical limits are reached, leading to chaotic responses. Nevertheless, there are cases where chaotic responses occur when the limits are not reached. This conclusion points to the importance of a deep dynamical analysis for a proper origami design due to the system nonlinearities.

Declaration of competing interest

The authors declare the following financial interests/personal relationships which may be considered as potential competing interests: Marcelo A. Savi reports financial support was provided by National Council for Scientific and Technological Development. Marcelo A. Savi reports financial support was provided by Coordination of Higher Education Personnel Improvement. Marcelo A. Savi reports financial support was provided by Carlos Chagas Filho Foundation for Research Support of Rio de Janeiro State.

Data availability

Data will be made available on request.

Acknowledgements

The authors would like to acknowledge the support of the Brazilian Research Agencies CNPq (Conselho Nacional de Desenvolvimento Científico e Tecnológico), CAPES (Coordenação de Aperfeiçoamento de Pessoal de Nível Superior) and FAPERJ (Fundação Carlos Chagas Filho de Amparo à Pesquisa do Estado do Rio de Janeiro). The support of the AFOSR (Air Force Office of Scientific Research) is also acknowledged.

Appendix A

This appendix presents details of the formulation of the trigonometric relation related to the rigid waterbomb unit-cell. The plane-symmetric waterbomb unit-cell (the unit-cell halved by the plane of symmetry Π_2 contained in the xz-plane) is presented in Fig. A.1.

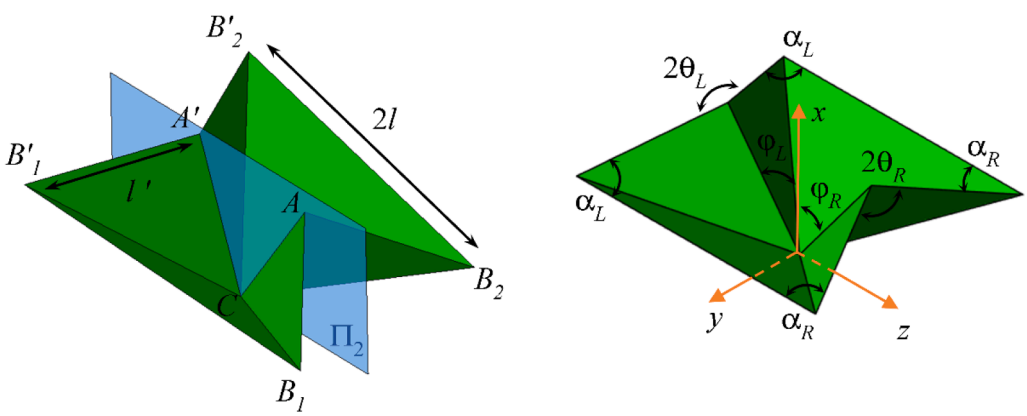

Fig. A.1. A plane-symmetric waterbomb unit-cell.

The unit-cell has lengths l and l' defined by $\overline{AC}$ and $\overline{AB_1}$, respectively. These lengths are interrelated to the angle λ such that $l' = l\tan\lambda$. In other words, if $\lambda = \pi/4$, $l = l'$ and the flat unit-cell is square.

The central vertex C is in the origin of the coordinate frame. The coordinates of the other vertices are given by:

$$A = l\begin{bmatrix}\cos\varphi_R\\ 0\\ \sin\varphi_R\end{bmatrix} \tag{A.1}$$

$$A' = l\begin{bmatrix}\cos\varphi_L\\ 0\\ -\sin\varphi_L\end{bmatrix} \tag{A.2}$$

$$B_1 = l\begin{bmatrix}\cos\varphi_R - \tan\lambda\cos\theta_R\sin\varphi_R\\ \tan\lambda\sin\theta_R\\ \sin\varphi_R + \tan\lambda\cos\theta_R\cos\varphi_R\end{bmatrix} \tag{A.3}$$

$$B'_1 = l\begin{bmatrix}\cos\varphi_L - \tan\lambda\cos\theta_L\sin\varphi_L\\ \tan\lambda\sin\theta_L\\ -\sin\varphi_L - \tan\lambda\cos\theta_L\cos\varphi_L\end{bmatrix} \tag{A.4}$$

$$B_2 = l\begin{bmatrix}\cos\varphi_R - \tan\lambda\cos\theta_R\sin\varphi_R\\ -\tan\lambda\sin\theta_R\\ \sin\varphi_R + \tan\lambda\cos\theta_R\cos\varphi_R\end{bmatrix} \tag{A.5}$$

$$B_2^{'} = l\begin{bmatrix} \cos\varphi_L - \tan\lambda\cos\theta_L\sin\varphi_L \\ -\tan\lambda\sin\theta_L \\ -\sin\varphi_L - \tan\lambda\cos\theta_L\cos\varphi_L \end{bmatrix} \tag{A.6}$$

The rigid origami model considers panel without deformation and, therefore, the length $\overline{B_1B_1^{'}}$ is constant and equal to $2l$. Thus, with aid of the equations Eq. (A.3) and Eq. (A.4), the following constraint equation is obtained:

$$(B_1 - B_1^{'}) = l\begin{bmatrix} \cos\varphi_R - \cos\varphi_L - \tan\lambda(\cos\theta_R\sin\varphi_R - \cos\theta_L\sin\varphi_L) \\ \tan\lambda(\sin\theta_R - \sin\theta_L) \\ \sin\varphi_R + \sin\varphi_L + \tan\lambda(\cos\theta_R\cos\varphi_R + \cos\theta_L\cos\varphi_L) \end{bmatrix}$$

$$4L^2 = |B_1 - B_1^{'}|^2$$

$$\begin{aligned} 4 \;=\; & (\tan\lambda\cos\varphi_R\cos\theta_R)^2 + 2(\tan\lambda)^2\cos\varphi_R\cos\varphi_L\cos\theta_R\cos\theta_L + (\tan\lambda\cos\varphi_L\cos\theta_L)^2 + (\tan\lambda\sin\varphi_L\cos\theta_L)^2 \\ & - 2(\tan\lambda)^2\sin\varphi_R\sin\varphi_L\cos\theta_R\cos\theta_L + (\tan\lambda\sin\varphi_R\cos\theta_R)^2 + 2\tan\lambda(\cos\varphi_R\sin\varphi_L\cos\theta_R + \cos\varphi_R\sin\varphi_L\cos\theta_L \\ + \;& \cos\varphi_L\sin\varphi_R\cos\theta_R + \cos\varphi_L\sin\varphi_R\cos\theta_L) + (\tan\lambda)^2\left[(\sin\theta_R)^2 - 2\sin\theta_R\sin\theta_L + (\sin\theta_L)^2\right] \\ + \;& (\cos\varphi_R)^2 - 2\cos\varphi_R\cos\varphi_L + (\cos\varphi_L)^2 + (\sin\varphi_R)^2 + 2\sin\varphi_R\sin\varphi_L + (\sin\varphi_L)^2 \end{aligned}$$

$$\begin{aligned} 2 \;=\; & (\tan\lambda)^2[\cos\varphi_R\cos\varphi_L\cos\theta_R\cos\theta_L - \sin\varphi_R\sin\varphi_L\cos\theta_R\cos\theta_L - \sin\theta_R\sin\theta_L + 1] \\ & + (\tan\lambda)[\cos\varphi_R\sin\varphi_L\cos\theta_R + \cos\varphi_R\sin\varphi_L\cos\theta_L + \cos\varphi_L\sin\varphi_R\cos\theta_R + \cos\varphi_L\sin\varphi_R\cos\theta_L] + 1 - \cos\varphi_R\cos\varphi_L + \sin\varphi_R\sin\varphi_L \end{aligned}$$

$$1 = (\tan\lambda)^2[\cos\theta_R\cos\theta_L\cos(\varphi_R + \varphi_L) - \sin\theta_R\sin\theta_L + 1] + (\tan\lambda)[\sin(\varphi_R + \varphi_L)(\cos\theta_R + \cos\theta_L)] - \cos(\varphi_R + \varphi_L)$$

Defining $\varphi_R + \varphi_L = 2\varphi$:

$$1 = (\tan\lambda)^2[\cos\theta_R\cos\theta_L\cos(2\varphi) - \sin\theta_R\sin\theta_L + 1] + (\tan\lambda)[\sin(2\varphi)(\cos\theta_R + \cos\theta_L)] - \cos(2\varphi) \tag{A.7}$$

Considering the symmetric case where $\theta_R = \theta_L = \theta$ in equation Eq. (A.7):

$$1 = (\tan\lambda)^2\left[(\cos\theta)^2\cos(2\varphi) - (\sin\theta)^2 + 1\right] + (\tan\lambda)[\sin(2\varphi)(2\cos\theta)] - \cos(2\varphi)$$

Replacing $\cos(2\varphi) = (\cos\varphi)^2 - (\sin\varphi)^2$ and $\sin(2\varphi) = 2\sin\varphi\cos\varphi$:

$$1 = (\tan\lambda)^2\left[(\cos\theta)^2\left(1 + (\cos\varphi)^2 - (\sin\varphi)^2\right)\right] + (\tan\lambda)[2\sin\varphi\cos\varphi(2\cos\theta)] - (\cos\varphi)^2 + (\sin\varphi)^2$$

$$2 = (\tan\lambda)^2\left[2(\cos\theta)^2(\cos\varphi)^2\right] + (\tan\lambda)[4\cos\theta\cos\varphi\sin\varphi] + 2(\sin\varphi)^2$$

$$1 = (\tan\lambda\cos\theta\cos\varphi + \sin\varphi)^2$$

Since θ, φ and λ are in the first quadrant:

$$1 = \tan\lambda\cos\theta\cos\varphi + \sin\varphi \tag{A.8}$$

Now, aiming to solve the equation Eq. (A.7) for φ, the following double-angle identities are considered:

$$\cos(2\varphi) = \frac{1 - (\tan\varphi)^2}{1 + (\tan\varphi)^2}$$

$$\sin(2\varphi) = \frac{2\tan\varphi}{1 + (\tan\varphi)^2}$$

By replacing these identities in Eq. (A.7):

$$1 = (\tan\lambda)^2\left[\cos\theta_R\cos\theta_L\frac{1 - (\tan\varphi)^2}{1 + (\tan\varphi)^2} - \sin\theta_R\sin\theta_L + 1\right] + (\tan\lambda)\left[\frac{2\tan\varphi}{1 + (\tan\varphi)^2}(\cos\theta_R + \cos\theta_L)\right] - \frac{1 - (\tan\varphi)^2}{1 + (\tan\varphi)^2}$$

$$0 = \left(\frac{1 - (\tan\varphi)^2}{1 + (\tan\varphi)^2}\right)\left[(\tan\lambda)^2\cos\theta_R\cos\theta_L - 1\right] + \left(\frac{2\tan\varphi}{1 + (\tan\varphi)^2}\right)[(\tan\lambda)(\cos\theta_R + \cos\theta_L)] + (\tan\lambda)^2(1 - \sin\theta_R\sin\theta_L) - 1$$

To simplify the next steps, the following replacements are given:

$$C_1 = (\tan\lambda)^2\cos\theta_R\cos\theta_L - 1$$

$$C_2 = (\tan\lambda)(\cos\theta_R + \cos\theta_L)$$

$$C_3 = (\tan\lambda)^2(1 - \sin\theta_R\sin\theta_L) - 1$$

Thus, a quadratic equation with unknown variable φ is obtained:

$$0 = \left(1 - (\tan\varphi)^2\right)C_1 + (2\tan\varphi)C_2 + C_3\left(1 + (\tan\varphi)^2\right)$$

$$0 = (\tan\varphi)^2(-C_1 + C_3) + (\tan\varphi)(2C_2) + (C_1 + C_3)$$

$$\tan\varphi = \frac{-(2C_2) \pm \sqrt{(2C_2)^2 - 4(-C_1 + C_3)(C_1 + C_3)}}{2(-C_1 + C_3)}$$

$$\tan\varphi = \frac{-(C_2) \pm \sqrt{C_2^2 - \left(-C_1^2 + C_3^2\right)}}{(-C_1 + C_3)}$$

Expanding the term $C_2^2 - (-C_1^2 + C_3^2)$:

$$\begin{aligned} C_2^2 \; - \; & \left(-C_1^2 + C_3^2\right) = (\tan\lambda)^2\left[(\cos\theta_R)^2 + (\cos\theta_L)^2 + 2\cos\theta_R\cos\theta_L\right] + (\tan\lambda)^4(\cos\theta_R)^2(\cos\theta_L)^2 + 1 - 2(\tan\lambda)^2\cos\theta_R\cos\theta_L \\ - \; & \left\{(\tan\lambda)^4\left[1 - 2\sin\theta_R\sin\theta_L + (\sin\theta_R)^2(\sin\theta_L)^2\right] + 1 - 2(\tan\lambda)^2(1 - \sin\theta_R\sin\theta_L)\right\} \end{aligned}$$

$$C_2^2 - \left(-C_1^2 + C_3^2\right) = (\tan\lambda)^4\left[(\cos\theta_R)^2(\cos\theta_L)^2 - 1 + 2\sin\theta_R\sin\theta_L - (\sin\theta_R)^2(\sin\theta_L)^2\right] + (\tan\lambda)^2\left[(\cos\theta_R)^2 + (\cos\theta_L)^2 + 2 - 2\sin\theta_R\sin\theta_L\right]$$

$$C_2^2 - \left(-C_1^2 + C_3^2\right) = (\tan\lambda)^2\left[4 - (\sin\theta_R + \sin\theta_L)^2 - (\tan\lambda)^2(\sin\theta_R - \sin\theta_L)^2\right]$$

Expanding the term $-C_1 + C_3$:

$$-C_1 + C_3 = (\tan\lambda)^2(1 - \sin\theta_R\sin\theta_L) - 1 - (\tan\lambda)^2\cos\theta_R\cos\theta_L + 1$$

$$-C_1 + C_3 = (\tan\lambda)^2[1 - \cos(\theta_R - \theta_L)]$$

Returning to the solution of the quadratic equation:

$$\tan\varphi = \frac{-(\tan\lambda)(\cos\theta_R + \cos\theta_L) \pm \sqrt{(\tan\lambda)^2\left[4 - (\sin\theta_R + \sin\theta_L)^2 - (\tan\lambda)^2(\sin\theta_R - \sin\theta_L)^2\right]}}{(\tan\lambda)^2[1 - \cos(\theta_R - \theta_L)]}$$

$$\tan\varphi = \frac{-(\cos\theta_R + \cos\theta_L) + \sqrt{\left[4 - (\sin\theta_R + \sin\theta_L)^2 - (\tan\lambda)^2(\sin\theta_R - \sin\theta_L)^2\right]}}{(\tan\lambda)[1 - \cos(\theta_R - \theta_L)]} \tag{A.9}$$

The equation Eq. (A.9) describes φ as a function of θ_R and θ_L. This function is only valid for the plane-symmetric case. Note that in the symmetric case where $\theta_R = \theta_L$, the denominator of equation Eq. (A.9) is equal to zero.

In order to find an equivalent function for the symmetric case, consider the equation Eq. (A.8). Replacing cos φ and sin φ by the half-angle identities:

$$1 = \tan\lambda\cos\theta\left[\frac{1 - \left(\tan\frac{\varphi}{2}\right)^2}{1 + \left(\tan\frac{\varphi}{2}\right)^2}\right] + \left[\frac{2\tan\frac{\varphi}{2}}{1 + \left(\tan\frac{\varphi}{2}\right)^2}\right]$$

$$1 + \left(\tan\frac{\varphi}{2}\right)^2 = \tan\lambda\cos\theta\left[1 - \left(\tan\frac{\varphi}{2}\right)^2\right] + 2\tan\frac{\varphi}{2}$$

$$\left(\tan\frac{\varphi}{2}\right)^2[1 + \tan\lambda\cos\theta] + \left(\tan\frac{\varphi}{2}\right)[-2] + (1 - \tan\lambda\cos\theta) = 0$$

$$\tan\frac{\varphi}{2} = \frac{2 \pm \sqrt{2^2 - 4(1 + \tan\lambda\cos\theta)(1 - \tan\lambda\cos\theta)}}{2(1 + \tan\lambda\cos\theta)}$$

$$\tan\frac{\varphi}{2} = \frac{2 \pm \sqrt{4(\tan\lambda\cos\theta)^2}}{2(1 + \tan\lambda\cos\theta)}$$

$$\tan\frac{\varphi}{2} = \frac{1 \pm \tan\lambda\cos\theta}{(1 + \tan\lambda\cos\theta)}$$

$$\tan\frac{\varphi}{2} = \frac{1 - \tan\lambda\cos\theta}{1 + \tan\lambda\cos\theta} \tag{A.10}$$

References

[1] V. Agarwal, K.W. Wang, On the nonlinear dynamics of a Kresling-pattern origami under harmonic force excitation, Extreme Mech. Lett. 52 (2022) 101653.

[2] A.R. Ahmed, O.C. Gauntlett, G. Camci-Unal, Origami-inspired approaches for biomedical applications, ACS omega 6 (1) (2020) 46–54.

[3] L.A. Bowen, C.L. Grames, S.P. Magleby, L.L. Howell, R.J. Lang, A classification of action origami as systems of spherical mechanisms, J. Mech. Des. 135 (11) (2013).

[4] J.T. Bruton, T.G. Nelson, T.K. Zimmerman, J.D. Fernelius, S.P. Magleby, L. L. Howell, Packing and deploying soft origami to and from cylindricalvolumes with application to automotive airbags, R. Soc. Open Sci. 3 (9) (2016) 160429.

[5] Y. Chen, H. Feng, J. Ma, R. Peng, Z. You, Symmetric waterbomb origami, Proc. R. Soc.A: Math. Phys. Eng. Sci. 472 (2190) (2016) 20150846.

[6] Y. Chen, H. Feng, J. Ma, R. Peng, Z. You, Symmetric waterbomborigami, Proc. R. Soc. A: Math. Phys. Eng. Sci. 472 (2190) (2016) 20150846.

[7] M. Eidini, G.H. Paulino, Unraveling metamaterial properties in zigzagbase folded sheets, Sci. Adv. 1 (8) (2015) e1500224.

[8] A.A. Evans, J.L. Silverberg, C.D. Santangelo, Lattice mechanics oforigami tessellations, Phys. Rev. E 92 (1) (2015) 013205.

[9] H. Fang, S.C.A. Chu, Y. Xia, K.W. Wang, Programmable self-locking origami mechanical metamaterials, Adv. Mater. 30 (15) (2018) 1706311.

[10] L.J. Fei, D. Sujan, Origami theory and its applications: a literature review, World Acad. Sci. Eng. Technol. (2013) 1131–1135.

[11] H. Feng, J. Ma, Y. Chen, Z. You, Twist of tubular mechanical metamaterials based on waterbomb origami, Sci. Rep. 8 (1) (2018) 1–13.
[12] E.T. Filipov, G.H. Paulino, T. Tachi, Origami tubes with reconfigurable polygonal cross-sections, Proc. R. Soc. A: Math. Phys. Eng. Sci. 472 (2185) (2016) 20150607.
[13] L.M. Fonseca, M.A. Savi, Nonlinear dynamics of an autonomous robot with deformable origami wheels, Int. J. Non Linear Mech. 125 (2020) 103533.
[14] L.M. Fonseca, M.A. Savi, On the symmetries of the origami waterbomb pattern: kinematics and mechanical investigations, Meccanica 56 (10) (2021) 2575–2598.
[15] L.M. Fonseca, G.V. Rodrigues, M.A. Savi, An overview of the mechanical description of origami-inspired systems and structures, Int. J. Mech. Sci. 223 (2022) 107316.
[16] L.M. Fonseca, G.V. Rodrigues, M.A. Savi, A. Paiva, Nonlinear dynamics of an origami wheel with shape memory alloy actuators, Chaos Solitons Fractal. 122 (2019) 245–261.
[17] E.A.P. Hernandez, D.J. Hartl, D.C. Lagoudas, Active Origami, Springer, 2019.
[18] E.A.P. Hernandez, D.J. Hartl, R.J. Malak Jr, D.C Lagoudas, Origami-inspired active structures: a synthesis and review, Smart Mater. Struct. 23 (9) (2014) 094001.
[19] R. Imada, T. Tachi, Geometry and kinematics of cylindrical waterbomb tessellation, J. Mech. Robot. 14 (4) (2022) 041009.
[20] K. Kuribayashi, K. Tsuchiya, Z. You, D. Tomus, M. Umemoto, T. Ito, M. Sasaki, Self-deployable origami stent grafts as a biomedical application of Ni-rich TiNi shape memory alloy foil, Mater. Sci. Eng.: A 419 (1-2) (2006) 131–137.
[21] R.J. Lang, The science of origami, Phys. World 20 (2) (2007) 30.
[22] R.J. Lang, Twists, Tilings, and Tessellations: Mathematical Methods for Geometric Origami, AK Peters/CRC Press, 2017.
[23] D.Y. Lee, G.P. Jung, M.K. Sin, S.H. Ahn, K.J. Cho, Deformable wheel robot based on origami structure, in: 2013 IEEE International Conference on Robotics and Automation, 2013, pp. 5612–5617.
[24] J. Li, Q. Li, T. Sun, Z. Zhu, Z. Deng, A general formulation for simulating the dynamic deployment of thick origami, Int. J. Solids Struct. 274 (2023) 112279.
[25] S. Li, J.J. Stampfli, H.J. Xu, E. Malkin, E.V. Diaz, D. Rus, R.J. Wood, A vacuum-driven origami "magic-ball" soft gripper, in: 2019 International Conference on Robotics and Automation (ICRA), IEEE, 2019, pp. 7401–7408.
[26] H. Liu, P. Plucinsky, F. Feng, R.D. James, Origami and materialsscience, Philos. Trans. R. Soc. A 379 (2201) (2021) 20200113.
[27] J. Ma, Z. You, Modelling of the waterbomb origami pattern and its applications, in: International Design Engineering Technical Conferences and Computers and Information in Engineering Conference 46377, American Society of Mechanical Engineers, 2014. V05BT08A047.
[28] J. Ma, H. Feng, Y. Chen, D. Hou, Z. You, Folding of tubular waterbomb, Research (2020) 2020.
[29] C.B. Mathew, M. Raikwar, M.S. Negi, H. Singh, Compliant mechanism and origami usage in aerospace and space application, in: IOP Conference Series: Earth and Environmental Science 775, IOP Publishing, 2021 012008.
[30] N.A. Megahed, Origami folding and its potential for architecture students, Desig. J. 20 (2) (2017) 279–297.
[31] M. Meloni, J. Cai, Q. Zhang, D. Sang-Hoon Lee, M. Li, R. Ma, T.E. Parashkevov, J Feng, Engineering origami: a comprehensive review of recent applications, design methods, and tools, Adv. Sci. 8 (13) (2021) 2000636.
[32] Y. Pang, X. Zhu, Y. Yu, S. Liu, Y. Chen, Y. Feng, Waterbomb-origami inspired triboelectric nanogenerator for smart pavement-integrated traffic monitoring, Nano Res. (2022) 1–11.
[33] G.V. Rodrigues, M.A. Savi, Reduced-order model description of origami stent built with waterbomb pattern, Int. J. Appl. Mech. 13 (02) (2021) 2150016.
[34] G.V. Rodrigues, L.M. Fonseca, M.A. Savi, A. Paiva, Nonlinear dynamics of an adaptive origami-stent system, Int. J. Mech. Sci. 133 (2017) 303–318.
[35] P.W. Rothemund, Folding DNA to create nanoscale shapes and patterns, Nature 440 (7082) (2006) 297–302.
[36] N. Turner, B. Goodwine, M. Sen, A review of origami applications in mechanical engineering, Proc. Inst. Mech. Eng., Part C: J. Mech. Eng. Sci. 230 (14) (2016) 2345–2362.
[37] Y. Xia, N. Kidambi, E. Filipov, K.W. Wang, Deployment dynamics of Miura origami sheets, J. Comput. Nonlinear Dyn. 17 (7) (2022) 071005.